Sustainable Energy & Fuels

ROYAL SOCIETY OF CHEMISTRY

PAPER

View Article Online
View Journal

Cite this: DOI: 10.1039/d5se01070e

Facet-dependent photocatalytic activities of BiOBr explored through pattern illumination time-resolved phase microscopy

Yuta Egawa,[a] Yuanyuan Jiang,[b] Zhenhua Pan,[c] Sheng Ye [b] and Kenji Katayama [a]*

This study presents a detailed investigation into the photocatalytic properties of facet-engineered bismuth oxybromide (BiOBr) using the pattern illumination time-resolved phase microscopy (PI-PM) technique. BiOBr, recognized for its excellent visible-light photocatalytic capabilities, was synthesized with controlled facet exposure to enhance its reactivity and efficiency in degrading organic pollutants. The experimental focus was on assessing the facet-dependent behavior of photo-excited charge carriers within BiOBr under various scavenger conditions. The PI-PM method allowed for the direct imaging of dynamic charge carrier processes at the microscale, offering information on the active charge carrier types (electrons and holes) on the photocatalyst surface. Detailed analyses when exposed to scavengers revealed distinct behaviors across different facets (001, 010, and 102). Key findings include the identification of dominant charge carriers responsible for the enhanced photocatalytic activity of different facets. For instance, the (010) facet showed a pronounced reactivity of holes, whereas the (102) facet was predominantly active *via* electron-mediated processes. This facet-specific activity underlines the importance of surface properties in optimizing photocatalytic efficiency. Through the application of PI-PM, this research not only provides a deeper understanding of the mechanistic pathways in photocatalysis but also demonstrates the critical role of surface facets in determining the overall performance of BiOBr as a photocatalyst.

Received 7th August 2025
Accepted 13th November 2025

DOI: 10.1039/d5se01070e

rsc.li/sustainable-energy

Introduction

In recent years, the escalating concerns surrounding environmental pollution have driven the scientific community to explore innovative and efficient methods for the remediation of contaminated ecosystems. Among the various strategies developed, photocatalytic materials have emerged as a promising avenue for the decomposition of contaminant molecules.[1] Leveraging the power of light, these materials initiate chemical reactions that break down pollutants into less harmful substances, offering a green and sustainable approach to environmental cleanup.

Among plenty of materials explored for photocatalytic applications, titanium dioxide (TiO_2) stands out as a standard, owing to its remarkable efficiency, stability, and environmental benignity. As a semiconductor, TiO_2 harnesses ultraviolet light to generate electron–hole pairs, which then initiate oxidative and reductive reactions capable of breaking down a wide variety of contaminant molecules into less harmful constituents. This photocatalytic ability of TiO_2 has been extensively applied in air and water purification, self-cleaning surfaces, and even in the degradation of complex organic pollutants,[2] and a mechanistic study has been performed.[3] The versatility of TiO_2, coupled with its non-toxicity and abundance, underscores its pivotal role in advancing photocatalytic technology towards sustainable environmental remediation.

In the quest for efficient photocatalytic materials that operate under visible light, bismuth-based semiconductors have attracted significant attention, particularly for their unique electronic structures and favorable light absorption properties. Among these, bismuth vanadate ($BiVO_4$) emerges as a standout candidate, distinguished by its ability to harness visible light for the activation of photocatalytic processes.[4,5] Compared with typical metal oxide materials, its valence band is mixed with 6s of bismuth and 2p of oxide, shifting the valence band upward.[6] This capability is crucial for environmental applications where sunlight is the primary energy source. $BiVO_4$ and other bismuth-incorporated materials demonstrate remarkable proficiency in degrading organic pollutants and in water splitting applications, showcasing their potential as versatile and effective photocatalysts for environmental remediation. Besides $BiVO_4$, BiOX (X = Cl, Br, I) materials stand out in the realm of

[a]Department of Applied Chemistry, Chuo University, Tokyo 112-8551, Japan. E-mail: kkata.33g@g.chuo-u.ac.jp; Tel: +81-3-3817-1913

[b]College of Science & School of Plant Protection, State Key Laboratory of Tea Plant Biology and Utilization, Anhui Agricultural University, Shushan District, Hefei, Anhui, 230036, China

[c]Department of Applied Chemistry, Graduate School of Engineering, University of Hyogo, Himeji, Hyogo 671-2280, Japan

photocatalysts due to their unique properties and advantages. These materials exhibit superior photocatalytic properties, enabling the degradation of organic dyes and hazardous gases and even enabling sterilization and hydrogen photoelectrolysis, exceeding the ability of the standard TiO_2 photocatalyst, P25. Their superior performance can be attributed to their suitable band gap and well-dispersed valence band, which make them highly responsive to visible light.[7–9] In recent years, the facet-selective synthesis for BiOX could further improve the photocatalytic activity.[10,11]

To understand the photocatalytic activity, not only the reaction rate or yield, but also the reaction sources and photo-excited electron and hole dynamics are important because they are the origin of the reactions, although the following reactions include various active oxygen species, such as hydroxyl radicals, superoxide anions, *etc.*[12] We have developed a new measurement technique, called pattern illumination time-resolved phase microscopy (PI-PM), to study the reaction dynamics of photocatalytic and photovoltaic materials. In this technique,[13] we are able to directly image the sample surface with high time resolution *via* the refractive index change due to the photogenerated charge carriers. The subtle image change can be recovered by informatics calculations and categorized according to different types of carrier dynamics. This method enables the observation of photo-excited charge carrier dynamics through changes in the refractive index, rather than through alterations in transient absorption or photoluminescence.[14–16] Observing changes in the refractive index is particularly advantageous for examining non-radiative relaxation processes, involved in processes such as charge diffusion, entrapment in defect/surface states, and interfacial charge transfer.[17–20] In this way, the location-dependent carrier behavior on a surface can be mapped. This method could distinguish the reactive electrons and holes for TiO_2, hematite, and other photocatalytic photovoltaic materials[21,22] and also the active sites of co-catalysts based on the charge carrier behavior.[23,24] For the assignment of the charge carriers, the charge carrier type map was used and compared with and without scavengers, clarifying the reactivity of electrons and holes at each location.[25] The reaction sites for electrons and holes are spatially separated on the micron scale, which was unexpected because the typical sizes of photocatalytic materials were tens or hundreds of nanometers.

In this study, a BiOBr photocatalyst was synthesized by facet engineering to study its promising photocatalytic activities for the decomposition of organic molecules, and the dominant charge carriers for the photocatalytic degradation reactions were confirmed. The origin of the carrier behavior was investigated by the PI-PM method to clarify how the reactive carriers are distributed on each facet.

Methods

Pattern-illumination time-resolved phase microscopy

Previous studies have laid the groundwork for understanding the PI-PM technique,[22,26] and the principle, methods, features and applications are summarized in our recent review paper.[13] Briefly, this is a time-resolved pump–probe microscopy method where the pump and probe light are collimated to illuminate the sample surface with a diameter of ~0.5 mm and the pump-induced change (photo-excitation of charge carriers) is observed *via* a phase-contrast microscope, namely a refractive index change by adjusting a slightly modified focus point.[27] Both the pump and probe lights are pulsed lights with a pulse width of a few nanoseconds, and the time-resolved image can be obtained by controlling the timing of the two pulses. An arbitrary pump light pattern is used to photoexcited charge carriers within the sample. These carriers are then subjected to processes such as charge trapping, recombination, and transfer, leading to their generation and temporal decay. The spatial distribution of the photoexcited charge carriers is visualized through refractive index changes, captured using the phase contrast imaging. There are several key points to this method: the noisy image due to pulse-light imaging is recovered by mathematical and statistical calculations called "total-variation regularization"; the carriers trapped at the surface/defect states are efficiently observed by refractive index detection, which are not observed directly by transient absorption or time-resolved photoluminescence; different types of carriers on a surface are distinguished by the sign of the refractive index change and the distribution change due to scavengers (electrons/holes).

The setup employs a digital micro-mirror device (DMD) to project a distinct light pattern onto a sample, stimulating the generation of charge carriers within the material. As time progresses, these photo-induced charge carriers experience various decay mechanisms, such as trapping, recombination, and transport, which alter the refractive index of the sample.[27,28] The images obtained under pulse-light illumination have large inhomogeneous fluctuation in intensity, and the image sequence was processed using three-dimensional total variation regularization (x, y, and time) to enhance the signal-to-noise ratio (S/N), while preserving the structural integrity of the images. During this process, the image contrast under pump light illumination/non-illumination is necessary, and thus pattern illumination is necessary for this purpose.[29] The PI-PM's optical setup can be found in Fig. S1 in the SI. For our experimental procedures, we utilized a striped light pattern as the pump light, uniformly spaced horizontally across the sample and focusing analysis on the sensor's central area. The striped pattern had dimensions of 14.1 and 93.9 μm, with the total image size being 480.8 × 93.9 μm, corresponding to a resolution of 1024 × 200 pixels and a pixel width of 469 nm. The pump light originated from the third harmonic of a Nd:YAG pulse laser (3 ns pulse width, 355 nm wavelength) provided by a GAIA, Rayture Systems, while the probe light came from the second harmonic of another Nd:YAG pulse laser (3 ns pulse width, 532 nm wavelength). The diameter of the area irradiated by the pump pulse was 0.5 mm. The pump light intensity was 0.8 mJ per pulse, and the probe light intensity was 0.02 mJ per pulse, respectively. The microscopy technique achieved an optical resolution between 2 and 3 μm. The repetition of the pump pulse light was 0.5 Hz, and the signal is fully recovered after each pump pulse is irradiated.

The bandgap energy of BiOBr is higher than the probe energy, as shown in Fig. S2, but the transient absorption responses can be included in the image. But the amplitude of the transient absorption response was much weaker than the refractive index change in this case, which can be confirmed by adjusting the sample position at the focal plane. The refractive index change is enhanced by adjusting the focus position slightly away from the focal plane, while the transient absorption response does not change. Under our microscopic setup, the transient absorption response was not detected.

Clustering analysis

In the PI-PM method, the classification of the charge carrier types on a surface is indicated by clustering analysis.[13] In the study, specific areas within the 20 × 32 μm pump-light illuminated region were selected for detailed examination of the samples. The PI-PM technique was used to acquire time-varying signals at each pixel within this designated area, consisting of >10 000 response curves at each local position in the images. Each response corresponds to 100–200 signal intensities ranging from nanoseconds to milliseconds. These response curves were then analyzed and grouped by the clustering analysis. In general, cluster analysis refers to a family of multivariate statistical techniques used to group data points into categories (clusters) based on their degree of similarity, without predefined labels. In our case, each time-resolved PI-PM signal (represented as a numerical vector of 100–200 intensities over time) was grouped according to similarity using spectral clustering, which identifies natural groupings in the data by analyzing the eigen structure of a similarity matrix. This enabled us to classify >10 000 local responses into distinct categories that reflect different types of carrier dynamics. Outliers were then removed by manual inspection, and the categorized results were mapped back onto the optical image to visualize the spatial distribution of the charge-carrier responses. Following this classification, a map showing the positions of the categorized responses on an optical image was created, allowing the spatial distribution of the different types of responses to be visualized, corresponding to different types of "charge carriers".

Sign of refractive index change

For most materials, a probe wavelength of 532 nm is longer than the absorption edge of the band gap. In such cases, the contribution of the refractive index due to optical transitions is minimal. The PI-PM method, however, can often detect trapped charge carriers at the interface through changes in the refractive index. This phenomenon is attributed to the accumulation of charges at the interface, which generates a localized electric field, E_{local}. If the surface charge density is σ, the electric field near the interface is given by

$$E_{local} = \frac{\sigma}{\varepsilon_r \varepsilon_0}, \quad (1)$$

where σ is the surface charge density, ε_r is the relative permittivity of the material, and ε_0 is the permittivity of free space. The direction of E_{local} depends on the type of charge: $\sigma > 0$ for holes and $\sigma < 0$ for electrons. This local electric field modifies the material's permittivity (ε) through the electro-optic relationship.

$$\Delta\varepsilon = -\varepsilon_r{}^2 r E_{local}, \quad (2)$$

where r is the Pockels coefficient. For holes, the permittivity increases, whereas for electrons, it decreases. The $\varepsilon_r{}^2$ term arises due to the polarization response and the reduction of the local field within the dielectric medium. This effect can be understood as follows: electrons attract the electric field (causing the field to point toward the interface), leading to a reduction in permittivity and a phase advance of the electromagnetic wave, while holes have the opposite effect.

It is important to note that the Pockels effect here does not depend on the absence of centrosymmetry like in the bulk crystal structure. Instead, photoexcitation generates localized charges (electrons or holes) that accumulate at specific sites such as interfaces, grain boundaries, or defects. These localized charges break the symmetry in their immediate vicinity, even if the bulk material remains centrosymmetric.

The phase change caused by the refractive index modification (Δn) is theoretically described as

$$\Delta n \cong \frac{\Delta\varepsilon}{2n}, \quad (3)$$

This relation comes from the relationship of $(n + \Delta n) \cong (\varepsilon + \Delta\varepsilon)^2$ when Δn and $\Delta\varepsilon$ are small. This relationship indicates that the refractive index change caused by photo-excited electrons and holes has opposite signs within the same material environment. This distinction is valuable for identifying the type of charge carrier: if one response is attributed to electrons, the response with the opposite sign can be confidently assigned to holes, and *vice versa*.

Measurement cell

A glass substrate holding a film sample was sandwiched with another glass substrate, separated by a 0.5 mm thick rubber spacer to form a liquid layer over the film. The gap was filled with acetonitrile (ACN), ethanol (EtOH), and a mixture containing 0.1 mM nitrobenzene (NB) in EtOH. ACN was selected for its role as an inert liquid, noted for its inability to facilitate charge transfer from the photocatalytic materials to the liquid. On the other hand, EtOH served to scavenge holes, and the NB/EtOH solution acted as a scavenger for both electrons and holes. In environments for hole scavenging (using ethanol), NB was observed to convert into nitrosobenzene through the reduction reaction.[30] Identifying a perfect scavenger specifically for electrons under pulse-light conditions was found to be complex. Typical electron scavengers, like Ag^+, would experience photoreduction, resulting in nanoparticle formation on the substrates and affecting the signal's accuracy. Similarly, Fe^{3+} was deemed inappropriate as a scavenger due to its colored properties that absorb the pump light. This is the reason why the typical scavengers are not used in the study using the PI-PM method.

Preparation of samples

Preparation of BiOBr-(001), (010) and (102) nanosheets. All BiOBr nanosheets were synthesized through a hydrothermal reaction within a 100 mL polytetrafluoroethylene autoclave. The exposed facets of the nanosheets were manipulated by varying the composition of the precursor solution and the reaction conditions. Specifically, for the fabrication of BiOBr-(001), (010), and (102) nanosheets, the following precursor solutions and reaction conditions were employed, respectively. BiOBr-(001) nanosheets were fabricated using $Bi(NO_3)_3 \cdot 5H_2O$ (0.485 g) and cetyltrimethylammonium bromide (CTAB) (0.8 g) dissolved in 20 mL of deionized water and 1 mL of ethanol, and the reaction was conducted at 180 °C for 24 hours. BiOBr-(010) nanosheets were fabricated using $Bi(NO_3)_3 \cdot 5H_2O$ (1.94 g) and NaBr (0.412 g) dissolved in 60 mL of distilled water with the pH adjusted to 6.0 using 1 M NaOH, and the reaction was conducted at 160 °C for 24 hours. BiOBr-(102) nanosheets were fabricated using $Bi(NO_3)_3 \cdot 5H_2O$ (1.954 g) and KBr (0.476 g) dissolved in 80 mL of deionized water and 4 mL of ethanol, and the reaction was carried out at 180 °C for 24 hours. Following synthesis, the resulting particles were collected by centrifugation, rinsed with deionized water, and subsequently dried.

For PI-PM measurements, BiOBr particles were immobilized on a glass substrate by binding the particles to a glass substrate with heat treatment. Briefly, 1 mg of particles was dispersed in isopropanol (100 μL) by sonication. The suspension was then added dropwise onto a glass substrate (2 × 2 cm) and dried naturally in air. The particle/glass sample was annealed at 200 °C for 1 h under a flow of N_2 (200 mL min^{-1}). For both average and local response measurements, a sample film on a substrate was sandwiched between another piece of glass substrate with a 0.5 mm rubber spacer.

The photocatalytic degradation of glyphosate by BiOBr particles was conducted under visible light irradiation. Glyphosate is a widely used herbicide that controls broadleaf weeds and grasses. There is a concern that extensive glyphosate use has resulted in increasing residues in soil and waterways, indirectly exerting harmful side effects. The light resource was a 350 W Xe lamp with an ultraviolet cutoff filter (CEL-HXF 300-T3 CEL-HXUV300-T3, Beijing China Education Au-light Co., Ltd, $\lambda > 420$ nm, light intensity = 100 mW cm^{-2}). All photocatalytic tests were conducted at 5 °C in a cylindrical reactor with a radius of 15 cm and a height of 9.5 cm. Typically, during the photocatalytic degradation experiments, the photocatalyst (25 mg) was dispersed in 100 mL of glyphosate solution (10 mg L^{-1}). The suspension solution was kept in the dark for 120 min to ensure that the glyphosate molecules were sufficiently adsorbed on the photocatalyst. During the degradation reaction, 3 mL of suspension was sampled and then filtered with a 0.22 μm membrane. The products in the solution were analyzed using an Alliance 1260 high performance liquid chromatograph (HPLC) equipped with a UV-vis diode array detector using a reverse-phase C18 column (2.6 μm, 100 × 4.6 mm, Phenomenex, Los Angeles, USA). The UPLC mobile phase contained solvent A (pH = 11, 0.4 mol L^{-1} phosphate buffer solution) and solvent B (100% methanol) and the injection volume was 10 μL and the flow rate was 1.0 mL min^{-1}. In the controlled experiments (scavenger effect) of photocatalytic degradation, isopropanol (IPA, 10 mL), methanol (MeOH, 10 mL), and $K_2Cr_2O_7$ (0.5 mM) were used as quenchers for hydroxyl radicals ($^{\bullet}OH$), photo-excited holes (h^+), and electrons (e^-), respectively.

Results

Material characterization

The crystal structure and exposed surface facets of the BiOBr nanosheets were initially characterized using X-ray diffraction (XRD). As shown in Fig. 1, all three variants display diffraction patterns typical of tetragonal BiOBr. However, significant variations in the intensity of specific peaks were observed. The BiOBr-(001) sample shows prominently enhanced signals at the (001), (002), and (004) planes, signifying that the (001) facet is predominantly exposed. In contrast, BiOBr-(010) and BiOBr-(102) samples exhibit stronger diffraction from the (102), (110), and (200) planes, along with a notably reduced (002)/(200) peak ratio, suggesting diminished (001) surface contribution and increased expression of lateral or stepped crystal facets.

Morphological analysis *via* scanning electron microscopy (SEM; Fig. 2) revealed consistently uniform, sheet-like nanostructures across all three samples. Further evidence of facet orientation was obtained through high-resolution transmission electron microscopy (HRTEM) coupled with selected-area electron diffraction (SAED) as shown in Fig. 3. For BiOBr-(001), lattice fringes with a spacing of 0.277 nm—corresponding to the (110) plane—were identified (Fig. 3b), and the associated SAED pattern featured an interplanar angle of 45° between the (110) and (200) planes (Fig. 3c), aligning with crystallographic expectations. In the BiOBr-(010) sample, the measured lattice spacings of 0.405 nm and 0.282 nm corresponded to the (002) and (102) planes, respectively (Fig. 3e), with the SAED pattern

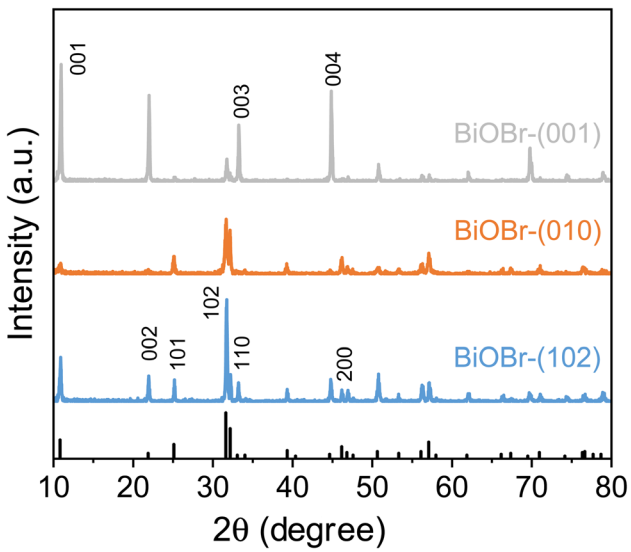

Fig. 1 XRD patterns for BiOBr with dominant facets: (001), (010) and (102).

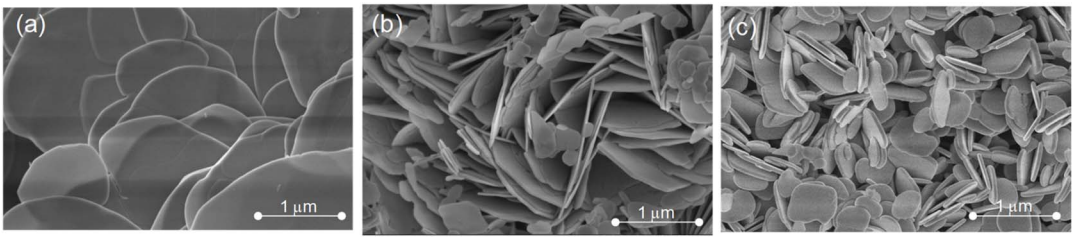

Fig. 2 SEM images of BiOBr with dominant facets: (a) (001), (b) (010) and (c) (102).

showing diffraction from the (102) and (004) planes separated by 45.9° (Fig. 3f). For BiOBr-(102), an additional lattice spacing of 0.173 nm was attributed to the (211) plane (Fig. 3h), and the corresponding SAED pattern displayed a ∼35° angle between diffraction spots (Fig. 3i), further confirming the dominance of the (102) facet.

We acknowledge that the photocatalytic activity of BiOBr nanosheets is affected not only by the dominant basal facets but also by the nature of the co-exposed edge facets, which can affect charge separation and surface reactivity.[31–33] In this study, for the sake of clarity and to facilitate discussion, we have referred to the samples based on their predominant exposed facets, without explicitly detailing the accompanying edge facets.

Degradation reactions and the scavenger effects

To clarify the active species in photocatalytic degradation, the scavenger effects were studied using the glyphosate degradation reaction. The results are shown in Fig. 4. The degradation ratios, C_i/C_0, were compared under different conditions. Without scavengers, the reaction efficiency was highest for the (102) facet, followed by the (010) and (001) facets. With respect to the (001) facet, the electron scavenger showed no effect, and the OH radical and hole scavenger reduced the reaction ratio, indicating that the active species are holes and OH radicals generated in the process of water oxidation by holes. The results were similar to those of the (010) facet, but the main active species was holes. The overall reaction ratios were larger for the (010) facet compared to the (001) facet. In contrast, the reaction

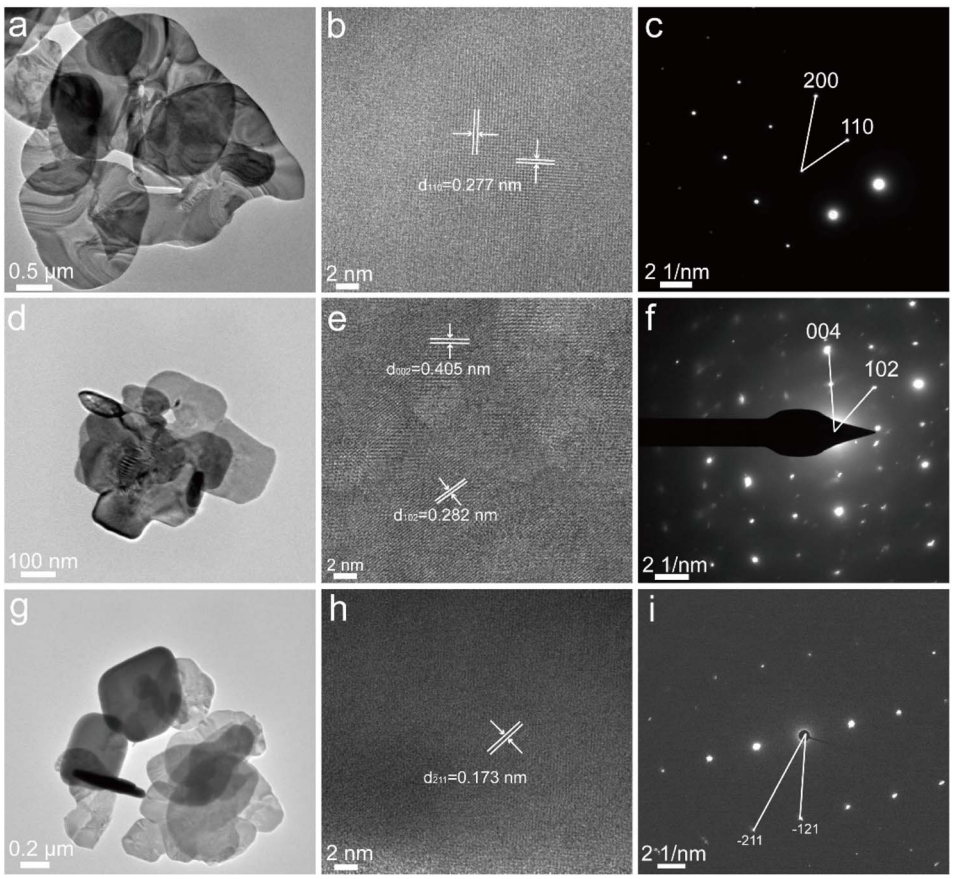

Fig. 3 HRTEM images and corresponding selected-area electron diffraction patterns of (a–c) BiOBr-(001), (d–f) BiOBr-(010) and (g–i) BiOBr-(102).

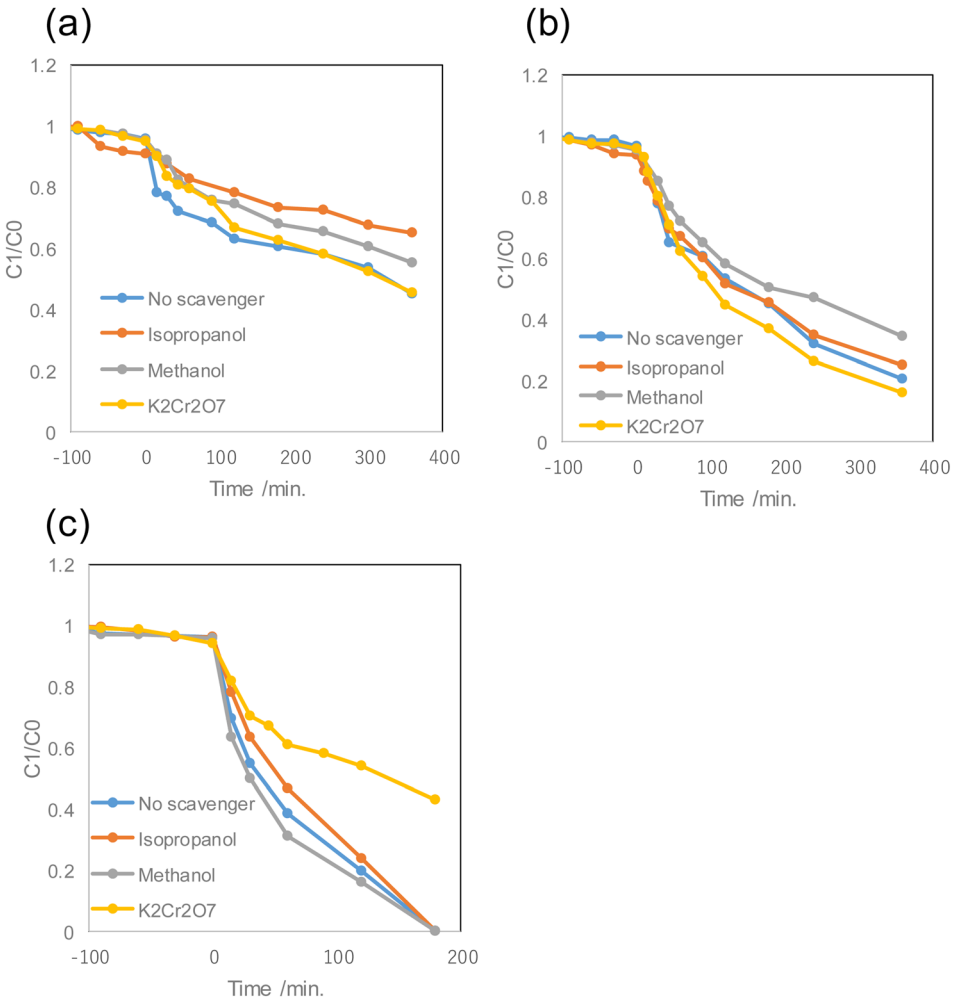

Fig. 4 The glyphosate degradation study of BiOBr with different facets: (a) (001), (b) (010), and (c) (102), respectively. The scavenger reagents were added at time zero. Isopropanol, methanol, and $K_2Cr_2O_7$ are used as scavengers for OH radicals, holes, electrons, and superoxide anions, respectively.

ratios were not affected by the hole or OH radical scavengers in the case of the (102) facet, and the electron scavenger greatly reduced the reaction ratio. This indicates that the active species for the (102) facet were photogenerated electrons. In general, electrons can be used for generating superoxide anions (O_2^- radicals), which have oxidation ability.[3] On the other hand, a pathway of direct reduction reactions is also known in some chemical species.[30]

PI-PM image sequences and time responses

To clarify the carrier behavior on each faceted surface, we measured each sample by the PI-PM method in contact with different liquids (inert (ACN), hole scavenger (EtOH), and electron/hole scavenger (NB/EtOH)). Fig. 5a–c show a time sequence of the images due to the refractive index change after pulsed pump irradiation for the (001), (010) and (102) faceted samples until 1000 μs, observed by the PI-PM method in acetonitrile (ACN). ACN works as an inert solvent, which prohibits interfacial charge transfer to the solvent, and Fig. S3 and S4 correspond to those in EtOH and NB/EtOH. The overall contrast of the excitation region became stronger until a few hundred nanoseconds, and it gradually decayed over a few tens of microseconds.

The average responses in the whole region were calculated by averaging the image intensities at all the pixels in the light-irradiated regions. The results for different facets and different scavenger solutions are shown in Fig. S5. In all the facets, the responses showed rise-and-decay responses with time constants of a few tens of nanoseconds for the rise and several microseconds for the decay for ACN and EtOH, and the signal intensities were smaller in EtOH, compared with those in ACN. In NB/EtOH, the response intensities became further smaller and both the rise and decay responses were delayed. In EtOH, the hole responses were scavenged; and, as a result, the signal intensities became smaller. In NB/EtOH, the number of charge carriers was reduced; as a result, the recombination became slower in general. In the previous papers,[17,28] particulate films often showed a response with a rising response on the order of nanoseconds in the refractive index change, followed by a decay on the order of microseconds. The rising response on

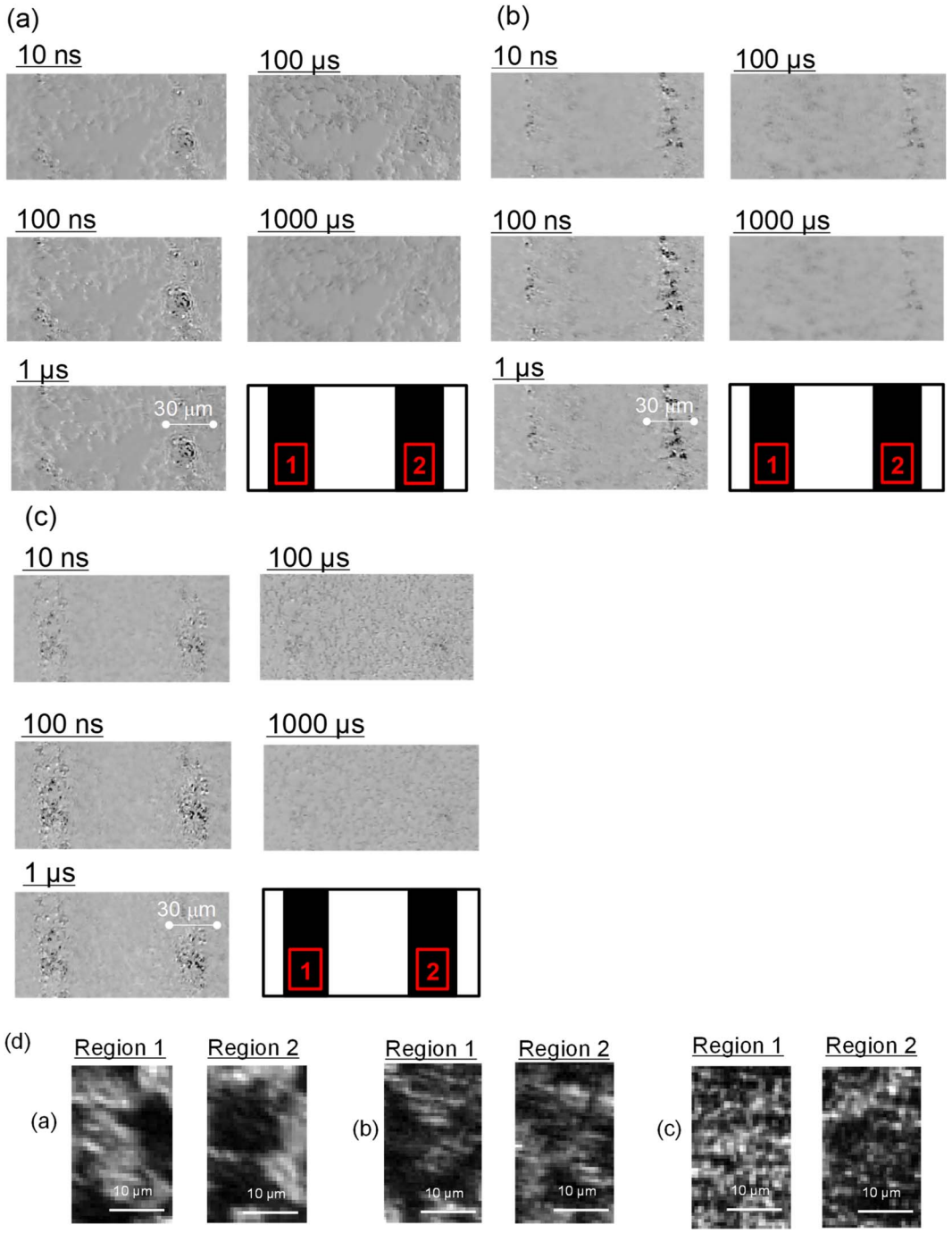

Fig. 5 The time-resolved image sequences of the refractive index changes under UV pump irradiation are shown for BiOBr with facets: (a) (001), (b) (010), and (c) (102) obtained by the time-resolved pattern-illumination phase microscopy (PI-PM) method in ACN. The light intensity patterns of the pump light are shown at the bottom of each image sequence (black rectangle: illuminated region), and the selected regions for the clustering analysis are indicated in red squares. (d) The expanded original optical image of the samples corresponding to the selected regions for (a–c) samples.

the order of nanoseconds was assigned due to the charge carrier trapping to the surface states, and the following decay corresponds to the recombination of charge carriers. Free carriers are first excited, which is often observed in the transient absorption response, typically in picoseconds to nanoseconds. However, the responses observed in the PI-PM method, *via* the refractive index change, increased the signal intensity on the order of tens to hundreds of nanoseconds, indicating that the charge carriers observed *via* the refractive index change are different from those observed by the transient absorption method. We found that this rising response is well explained by a model in which carrier diffusion accompanies trapping,[13] and is dominated by

the dynamic equilibrium between trapping and detrapping during diffusion, depending on the depth of the trap states.[24] The origin of the refractive index change at the interface is explained by the optical phase modulation by an increase/decrease of the electric field due to the accumulation of trapped carriers, as explained in the theory section. Still, the detailed processes are not clear from the average response, and we performed the clustering analysis in local regions for different scavenger solvents.

Two regions were analyzed by clustering for different faceted samples. (The regions are indicated in Fig. 5, S3 and S4 at the bottom.) One of the results for the (001) facet in region 1 is shown in Fig. 6. (The other region (region 2) is shown in Fig. S6 in the SI.) The results are shown as: (a) the image sequence of the analyzed region, (b) the category map of the different charge carriers, (c) the average charge carrier responses for each category, and (d) the time constants for each response. In ACN, we could find two categories of responses: rise-and-decay responses with the rise and decay time constants of 11 ± 1 ns and 2.0 ± 0.2 μs (red), and a single fall-and-recovery response with fall and recovery time constants of 14 ± 1 ns and 5.4 ± 0.6 μs (blue), and no response region (black). In EtOH, the decay times for the red and blue responses became faster, and the region of red decreased from 36 to 10%, while the blue region increased from 20 to 47%. In NB/EtOH, the blue responses drastically reduced to transition into the no response region (black), and the positive response has transitioned into a much slower response (green). In region 2, the general trend was similar but some differences were observed; the red responses became mostly no response (black) in the presence of ethanol (hole scavenger), and a small region with the blue response remained in NB/EtOH. With regard to the black region, there are two possibilities: one is the uncoated region and the other is the inactive photocatalyst coated due to unclear reasons. Since some regions became inactive due to scavengers, it indicates that the photocatalyst itself was coated in this case. Then, the latter possibility is more likely because many of these regions still provided signal responses in the absence of scavengers but became inactive when scavengers were introduced. Therefore, the black regions cannot be interpreted as empty substrates.

From the red area reduction by ethanol (Fig. 6A(b) and B(b)), the positive response (red) was due to the hole dynamics, because they were scavenged by EtOH. From the blue area reduction by addition of NB (Fig. 6B(b) and C(b)), the blue response corresponds to the electron dynamics because they were scavenged by NB. This makes sense because the sign of the refractive index change was opposite for electrons and holes. The green response was due to the hole dynamics from the sign, with residual signals persisting because hole scavenging is not fully efficient, especially for deeply trapped carriers. It is noted that holes are dominant on the surface when the charge carriers are confined inside the sample in ACN (inert), and this distribution of charge carriers did not directly correspond to the microscopy image, namely surface morphology. The difference between regions 1 and 2 can be considered due to the reaction activity, because the electron/hole responses were less scavenged in region 2 compared with those in region 1.

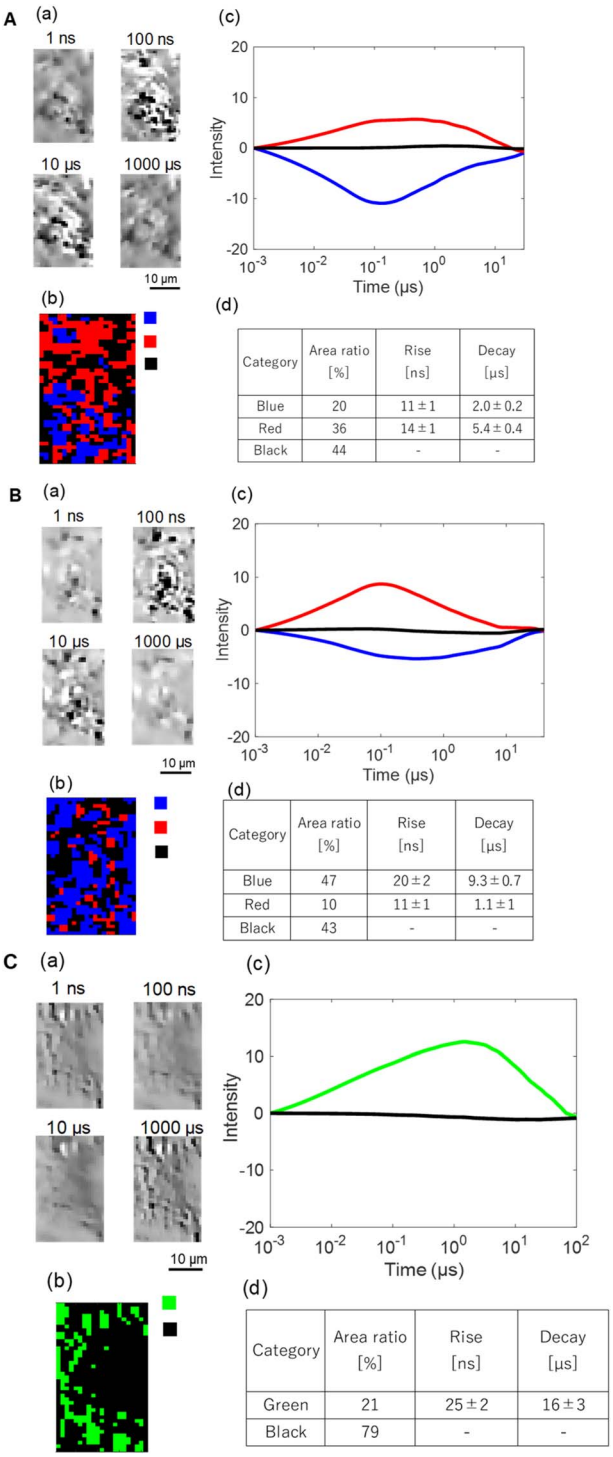

Fig. 6 The clustering analyses of the charge carrier responses of a BiOBr with the (001) facet in (A) ACN, (B) EtOH, and (C) NB/EtOH in region 1 of Fig. 5. (a) A microscopy image sequence and (b) the corresponding categorized map. (c) The averaged responses for the categorized responses. (d) The ratios of categories and the rise/decay times for the categories.

Next the results for the (010) facet are shown in Fig. 7 and S7. The results are similar to those for the (001) facet. In ACN, we could find two categories of responses: rise-and-decay

responses with the rise and decay time constants of 16 ± 1 ns and 11 ± 1 μs (red), and a fall-and-recovery response with fall and recovery time constants of 20 ± 1 ns and 4.6 ± 0.5 μs (blue), and no response region (black). In EtOH, all of the red response regions disappeared, while the region with the blue response did not change much. In NB/EtOH, the regions with the blue responses were reduced and they mostly transitioned into the no response region (black), and also a small slower response was observed (green). In region 2, the general trend was similar, except that the red region still remained a little in EtOH.

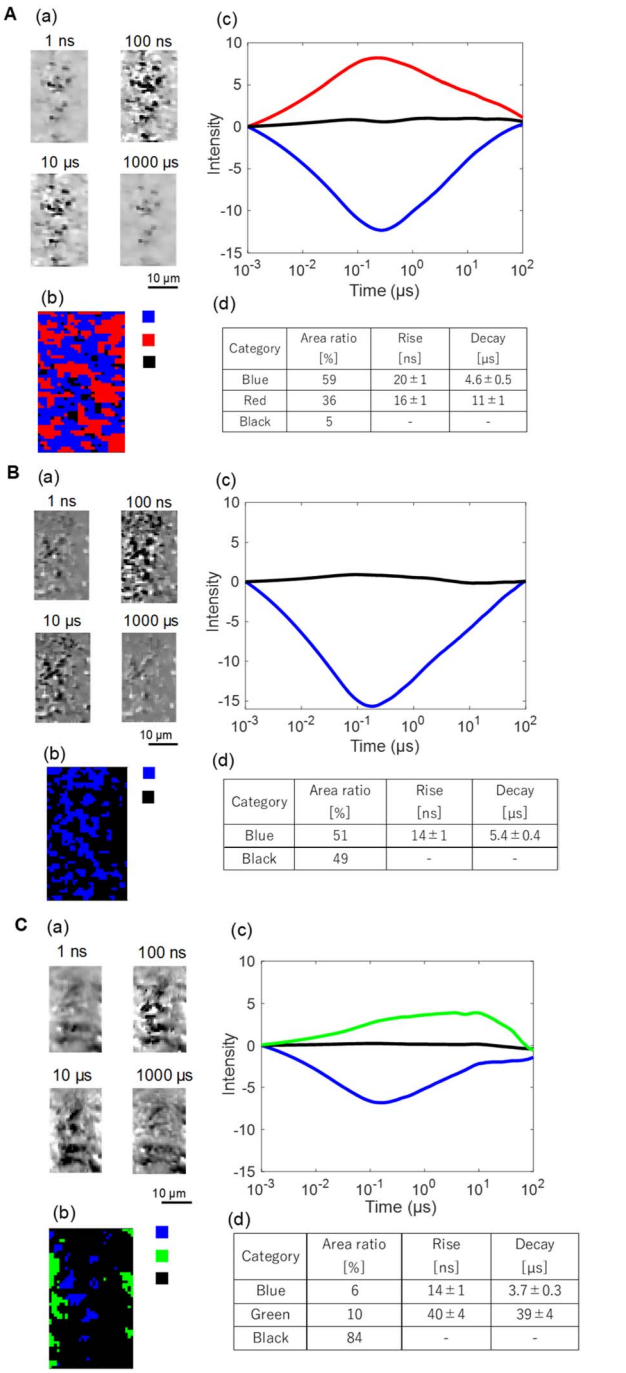

A

Category	Area ratio [%]	Rise [ns]	Decay [μs]
Blue	59	20 ± 1	4.6 ± 0.5
Red	36	16 ± 1	11 ± 1
Black	5	-	-

B

Category	Area ratio [%]	Rise [ns]	Decay [μs]
Blue	51	14 ± 1	5.4 ± 0.4
Black	49	-	-

C

Category	Area ratio [%]	Rise [ns]	Decay [μs]
Blue	6	14 ± 1	3.7 ± 0.3
Green	10	40 ± 4	39 ± 4
Black	84	-	-

Fig. 7 The clustering analyses of the charge carrier responses of BiOBr with the (010) facet in (A) ACN, (B) EtOH, and (C) NB/EtOH in region 1 of Fig. 5. (a) A microscopy image sequence, and (b) the corresponding categorized map. (c) The averaged responses for the categorized responses . (d) The ratios of categories and the rise/decay times for the categories.

From these results, the assignment of the colored regions was the same as the (001) faceted samples: red: holes, blue: electrons and green: delayed holes escaped from the recombination from the scavenger dependences. The minor difference between regions 1 and 2 was the effect of ethanol (hole scavenger), which was attributed to the hole reaction activity in each region. It is noted that the large difference between the (010) and (001) facets was the effect of the hole scavenger on the red region. In the case of the (010) facet, the scavenger effect of holes was significantly stronger than that for the (001) facet, as can be seen from the red region reduction by ethanol.

Next the results for the (102) facet are shown in Fig. 8 and S8. The results are similar to those for the other facets. In ACN, we could find two categories of responses: rise-and-decay responses with the rise and decay time constants of 14 ± 1 ns and 5.8 ± 0.6 μs (red), and a single valley-and-recovery response with fall and recovery time constants of 14 ± 1 ns and 1.3 ± 0.1 μs (blue), and no response region (black). In EtOH, the regions with the red response were reduced much, while the decay time for the blue response became much longer (1.3 to 22 μs). In NB/EtOH, the regions with the blue responses were reduced and mostly transitioned into the no response region (black), and also a slower positive response was observed (green). In region 2, the general trend was similar, except that the green response was observed in minor scattered regions in ACN and EtOH.

From these results, the assignment of the colored regions was also the same as the (001) and (010) facets: red: holes, blue: electrons and green: delayed holes escaped from the recombination from the scavenger dependence. The difference between regions 1 and 2 was that small regions showed a slower response regardless of the scavenger and possibly due to the less active trap states. The important point to note is that, different from the other facets, the blue region is dominant on the surface in ACN, and the lifetime of the electrons increases when holes are scavenged. The lifetime of the electrons became 10 times longer than that in ACN. Furthermore, the electron dynamics was clearly scavenged by NB.

Based on Fig. 5–7, we discussed the electron and hole dominant regions on the micron scale. However, the resolutions of the PI-PM and the SEM images have a large gap, and we cannot correspond to the optical (PI-PM) map with each faceted particle. What we can assert is that there are electron- or hole dominant regions on the micron scale. As shown in optical images corresponding to the measured area by the PI-PM method in Fig. 5–7, we do sometimes find some correspondence between the micron-scale morphology and the charge carrier map, but it is not always true and we cannot conclude the relationship between the morphology and the dominance of charge carriers.

The charge carrier behavior had a strong correlation with the photodegradation reactions shown in Fig. 4. The active species for the photodegradation were holes and OH radicals for the (010) and (001) facets, and the photodegradation efficiency for

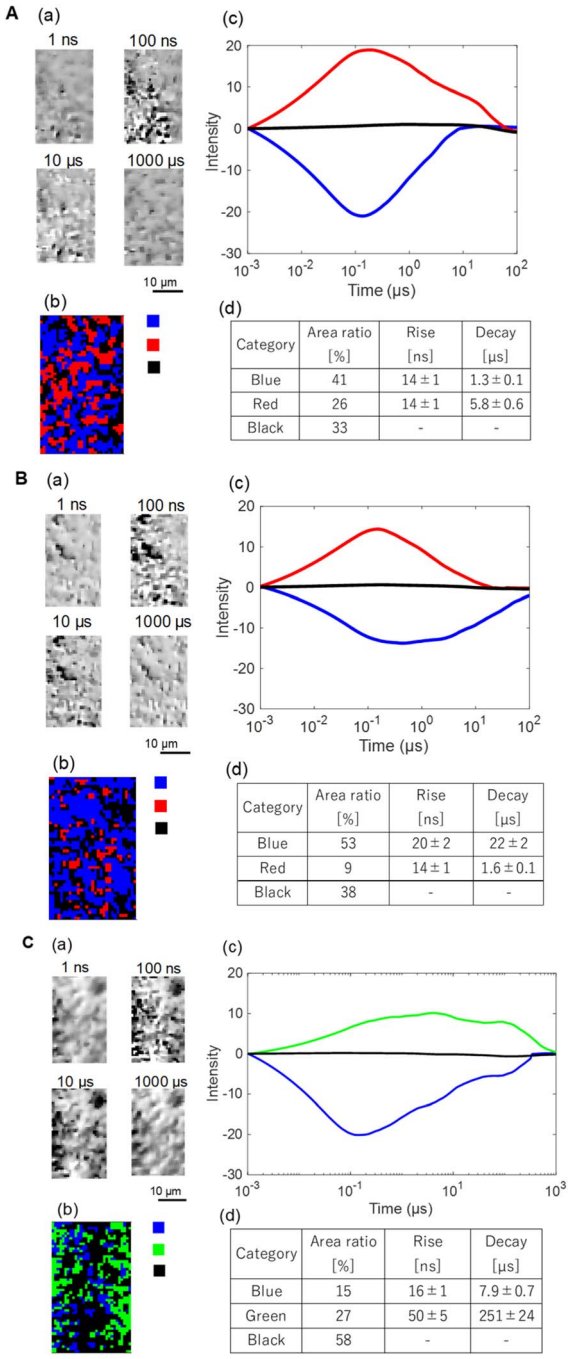

Fig. 8 The clustering analyses of the charge carrier responses of BiOBr with the (102) facet in (A) ACN, (B) EtOH, and (C) NB/EtOH in region 1 of Fig. 5. (a) A microscopy image sequence and (b) the corresponding categorized map. (c) The averaged responses for the categorized responses. (d) The ratios of categories and the rise/decay times for the categories.

the (010) facet was higher than that for the (001) facet. The active species for (001) and (010) facets were reflected on the surface map in ACN, where the holes (red regions) are dominant in the category map (Figure 6A and 7A). It is also indicated that the holes were scavenged more effectively at the (010) facet by EtOH (Fig. 6B) compared with the (001) facet (Fig. 7B), which indicates that the holes at the (010) facet have a stronger reaction ability and are easily scavenged.

On the other hand, the electron dynamics dominated the (102) facet from the charge carrier map in ACN (Fig. 8A), and this corresponds well to the active species for the (102) facet, which are electrons. Also, the elongation of the electron lifetime by removal of holes by the scavengers indicates that the electrons are able to react more efficiently in the alcohol solvents, by scavenging the holes. The electron activity for the (102) facet can be validated by taking the ratio between the regions of holes (red) and electrons (blue) in ACN. The average ratios for the regions of red and blue were 1 : 1.04, 1 : 2.28 and 1 : 3.14 for (001), (010) and (102), respectively, which indicated the (102) surface has stronger electron activity on the surface.

The study combined with the general degradation study with scavengers and the charge carrier type analysis by the PI-PM method provides clear information on the active charge carriers—not only the active charge types on the surface but also their lifetime variation. Along with this information, the facet engineered photocatalytic materials can be understood in terms of their reaction activity and its distribution. It is emphasized that this finding is possible when measured in ACN, which is not typically used in photocatalytic degradation reactions and has not been used in these studies; however, the contact of photocatalytic materials with ACN successfully confines the charge carriers inside the photocatalysts, which clearly indicates the active charge carriers. From this information of active carriers, we are able to understand the active species of the photocatalytic degradation reactions, using the PI-PM method.

Conclusion

We have explored the synthesis and characterization of bismuth oxybromide (BiOBr) photocatalysts engineered by facet control to optimize photocatalytic degradation reactions. The findings of this study contribute significantly to the understanding of photocatalyst behavior at the microscale in terms of active charge carrier types and their lifetimes and spatial distribution, through a novel PI-PM method.

BiOBr has demonstrated superior performance under visible light conditions compared to traditional photocatalysts such as TiO_2, primarily due to its favorable band gap and effective light absorption properties. Our findings emphasize that the facet-dependent behavior of BiOBr is critical in determining its photocatalytic activity. The facet-specific behavior of charge carriers—particularly how electrons and holes are influenced by the presence of scavengers—provides a deeper insight into the mechanistic pathways that govern the photocatalytic process. For instance, the varying responses to scavengers across different facets (001, 010, and 102) underline the importance of surface chemistry and structure in driving photocatalytic reactions.

The application of the PI-PM technique offers a microscopic distribution with a dynamic view of charge carrier behavior. This approach allows us to visualize and quantify the temporal and spatial distribution of photo-excited electrons and holes directly at the surface of photocatalysts. The ability to observe

these dynamics in real time presents a profound advancement in photocatalysis research, offering a more nuanced understanding of how photocatalytic materials behave under operational conditions.

Looking forward, the implications of this research are broad and impactful. The enhanced understanding of facet-dependent photocatalytic activity can guide the synthesis of more effective photocatalysts not only for environmental remediation but also for energy conversion processes, such as hydrogen production *via* water splitting. The methodologies developed here can be applied to other photocatalytic materials, potentially leading to breakthroughs in the design and application of photocatalysts.

Author contributions

KK designed the research, YE did the experiments and analyses, and YJ, ZP, SY prepared the samples and characterized them. YE, ZP and KK discussed and wrote the draft, and all the authors reviewed the manuscript.

Conflicts of interest

The authors have no competing interests or other interests that might be perceived to influence the results and/or discussion reported in this article.

Data availability

The data and figures generated and/or analyzed during the current study are available on request. The figures are open to the public under the condition that any use of the data is credited appropriately according to the citation guidelines provided.

Supplementary information: Fig. S1: setup of the PI-PM method, Fig. S2: image sequences of BiOBr for different facets in EtOH, Fig. S3: image sequences of BiOBr for different facets in NB/EtOH, Fig. S4: average time responses for all the facets of BiOBr in different scavenger solutions, Fig. S5: PI-PM analyses for the (001) facet of BiOBr in different scavenger solutions, Fig. S6: PI-PM analyses for the (010) facet of BiOBr in different scavenger solutions, and Fig. S7: PI-PM analyses for the (102) facet of BiOBr in different scavenger solutions. See DOI: **https://doi.org/10.1039/d5se01070e**.

Acknowledgements

The research was financially supported by JSPS KAKENHI (#22K05158), the Iketani Science and Technology Foundation, and the Institute of Science and Engineering, Chuo University.

References

1 W. S. Koe, J. W. Lee, W. C. Chong, Y. L. Pang and L. C. Sim, *Environ. Sci. Pollut. Res.*, 2020, **27**, 2522–2565.
2 D. Chen, Y. Cheng, N. Zhou, P. Chen, Y. Wang, K. Li, S. Huo, P. Cheng, P. Peng, R. Zhang, L. Wang, H. Liu, Y. Liu and R. Ruan, *J. Cleaner Prod.*, 2020, **268**, 121725.
3 N. Tsuchiya, K. Kuwabara, A. Hidaka, K. Oda and K. Katayama, *Phys. Chem. Chem. Phys.*, 2012, **14**, 4734–4741.
4 J. Chi, Z. Jiang, J. Yan, A. Larimi, Z. Wang, L. Wang and W. Shangguan, *Mater. Today Chem.*, 2022, **26**, 101060.
5 M. Malathi, J. Madhavan, M. Ashokkumar and P. Arunachalam, *Appl. Catal., A*, 2018, **555**, 47–74.
6 D. J. Payne, M. D. M. Robinson, R. G. Egdell, A. Walsh, J. McNulty, K. E. Smith and L. F. J. Piper, *Appl. Phys. Lett.*, 2011, **98**, 212110.
7 K.-L. Zhang, C.-M. Liu, F.-Q. Huang, C. Zheng and W.-D. Wang, *Appl. Catal., B*, 2006, **68**, 125–129.
8 L. Ye, Y. Su, X. Jin, H. Xie and C. Zhang, *Environ. Sci.: Nano*, 2014, **1**, 90–112.
9 A. Hussain, J. Hou, M. Tahir, S. S. Ali, Z. U. Rehman, M. Bilal, T. Zhang, Q. Dou and X. Wang, *Catal. Rev.*, 2024, **66**, 119–173.
10 X. Xiong, L. Ding, Q. Wang, Y. Li, Q. Jiang and J. Hu, *Appl. Catal., B*, 2016, **188**, 283–291.
11 X. Wu, Y. H. Ng, L. Wang, Y. Du, S. X. Dou, R. Amal and J. Scott, *J. Mater. Chem. A*, 2017, **5**, 8117–8124.
12 Y. Nosaka and A. Y. Nosaka, *Chem. Rev.*, 2017, **117**, 11302–11336.
13 K. Katayama, *Phys. Chem. Chem. Phys.*, 2024, **26**, 9783–9815.
14 T. J. Miao and J. Tang, *J. Chem. Phys.*, 2020, **152**, 194201.
15 J. Ma, T. J. Miao and J. Tang, *Chem. Soc. Rev.*, 2022, **51**, 5777–5794.
16 D. Friedmann, *Appl. Catal., A*, 2023, **649**, 118943.
17 K. Katayama, T. Chugenji and K. Kawaguchi, *Energies*, 2021, **14**, 7011.
18 M. Ebihara and K. Katayama, *J. Phys. Chem. C*, 2020, **124**, 23551–23557.
19 S. Kuwahara and K. Katayama, *Phys. Chem. Chem. Phys.*, 2016, **18**, 25271–25276.
20 S. Kuwahara, H. Hata, S. Taya, N. Maeda, Q. Shen, T. Toyoda and K. Katayama, *Phys. Chem. Chem. Phys.*, 2013, **15**, 5975–5981.
21 K. Katayama, K. Kawaguchi, Y. Egawa and Z. Pan, *Energies*, 2022, **15**, 9578.
22 M. Ebihara, T. Ikeda, S. Okunaka, H. Tokudome, K. Domen and K. Katayama, *Nat. Commun.*, 2021, **12**, 3716.
23 T. Chugenji, Z. Pan and K. Katayama, *J. Phys. Chem. C*, 2022, **126**, 19319–19326.
24 T. Chugenji, Z. Pan, V. Nandal, K. Seki, K. Domen and K. Katayama, *Phys. Chem. Chem. Phys.*, 2022, **24**, 17485–17495.
25 K. Kawaguchi, T. Chugenji, S. Okunaka, H. Tokudome and K. Katayama, *J. Phys. Chem. C*, 2022, **126**, 6646–6652.
26 K. Katayama, *J. Chem. Phys.*, 2020, **153**, 054201.
27 K. Katayama, T. Chugenji and K. Kawaguchi, *AIP Adv.*, 2021, **11**, 115215.
28 M. Ebihara, W. Y. Sohn and K. Katayama, *Rev. Sci. Instrum.*, 2019, **90**, 073905.
29 X. Huang, J. Fan, L. Li, H. Liu, R. Wu, Y. Wu, L. Wei, H. Mao, A. Lal, P. Xi, L. Tang, Y. Zhang, Y. Liu, S. Tan and L. Chen, *Nat. Biotechnol.*, 2018, **36**, 451–459.

30 K. Katayama, Y. Takeda, K. Shimaoka, K. Yoshida, R. Shimizu, T. Ishiwata, A. Nakamura, S. Kuwahara, A. Mase, T. Sugita and M. Mori, *Analyst*, 2014, **139**, 1953–1959.
31 R. Li, F. Zhang, D. Wang, J. Yang, M. Li, J. Zhu, X. Zhou, H. Han and C. Li, *Nat. Commun.*, 2013, **4**, 1432.
32 M. Shi, G. Li, J. Li, X. Jin, X. Tao, B. Zeng, E. A. Pidko, R. Li and C. Li, *Angew. Chem., Int. Ed.*, 2020, **59**, 6590–6595.
33 T. Liu, Z. Pan, J. J. M. Vequizo, K. Kato, B. Wu, A. Yamakata, K. Katayama, B. Chen, C. Chu and K. Domen, *Nat. Commun.*, 2022, **13**, 1034.

